PAPER

Check for updates

A sustainable and cost-effective industrial biomass-based coin cell supercapacitor for powering up electronic devices

Pooja Yadav,[ab] Sushil Patel,[ab] Gangadhar Mahar,[ab] W. Madhuri,[c] K. Rama Gopal[d] and P. Abdul Azeem ✩ *[ab]

Transforming industrial waste into an energy storage device addresses two key challenges: reducing industrial waste and providing a sustainable, low-cost material to meet global energy demands. In this study, the electrolyte material was optimized to create a high-performance supercapacitor using biomass by the sol−gel method. The prepared material exhibits a mesoporous structure with a specific surface area of 83.75 $m^2 g^{-1}$ and is used as a supercapacitor electrode material. Prior to the supercapacitor fabrication, selecting an optimal electrolyte is crucial for performance enhancement. The electrodes are electrochemically characterized with potassium hydroxide (KOH) and sodium hydroxide (NaOH) electrolytes. The 3.0 M KOH electrolyte is well-suited for electrochemical studies, exhibiting a low contact angle of 13° and a high conductivity of 146.2 $mS cm^{-1}$ with the nickel foam current collector. The electrode material achieved a high specific capacitance of 1590 $F g^{-1}$ at a current density of 3 $A g^{-1}$ using the 3.0 M KOH electrolyte. Additionally, the material is tested in a real-time coin cell supercapacitor device, which showed an excellent capacitance retention of 93% after 5000 cycles. The coin cell device demonstrated a high energy density of 10.66 $Wh kg^{-1}$ and a power density of 660 $W kg^{-1}$, enabling two cells in series to power a red-light emitting diode, a digital watch, and an electronic calculator.

1. Introduction

There is an urgency to develop efficient, ecologically friendly, and high-performance energy storage systems and devices because of the rapid depletion of fossil fuels and environmental concerns.[1,2] Researchers worldwide are exploring green and clean energy advancements to avoid fossil fuel consumption and mitigate their negative impacts.[3–6] There are various energy sources, such as water, wind, and solar energy, which are clean and renewable, but there are lots of challenges associated with them related to their temporal and weather-dependent availability.[7] As a result, it is essential to establish abundant energy storage technology that is independent of time and weather conditions. In confronting these difficulties, supercapacitors have emerged as important energy conversion devices.[8,9] They stand out for their rapid charge and discharge rates, extended cycle life, environmental sustainability, and high power density.[10,11] In addition, supercapacitors are divided into three

types according to their charge storage mechanisms: pseudo-capacitors (PCs), electric double-layer capacitors (EDLCs), and hybrid capacitors, which combine the characteristics of both PCs and EDLCs.[12] EDLCs store energy through an electrostatic, non-faradaic process, where electrons accumulate on the surface of the electrode material.[13,14] PCs, on the other hand, rely on a faradaic mechanism *via* redox reactions and store energy electrochemically.[15] Hybrid supercapacitors combine non-faradic and faradaic processes to provide a comprehensive energy storage solution.[16]

Meanwhile, waste management has always been a major concern, with contributions from a variety of sectors including electronics, agriculture, and industrial areas.[17] Recently, various breakthrough studies have been conducted for turning this waste into useful materials for electrochemical devices, particularly supercapacitors. Much of the research focuses on transforming waste into carbon-based materials such as carbon spheres, graphene, and carbon nanotubes. These materials are ideal for high-performance supercapacitors because of their exceptionally high specific surface area, porosity, stability, electrical conductivity, and capacitance.[18] The existing literature demonstrated the synthesis of biomass-based carbon materials from food, agricultural, or electronic waste, such as corncob residues, discarded watermelon rind, pineapple crowns, tea waste, waste tires, and solid leather waste.[19–21] However, there is limited research on the utilization of hazardous industrial wastes

[a]Department of Physics, National Institute of Technology, Warangal, Telangana, India. E-mail: drazeem2002@nitw.ac.in

[b]Centre of Excellence Glass Science and Technology, National Institute of Technology, Warangal, Telangana, India

[c]Centre for Functional Materials, Vellore Institute of Technology, Vellore 632014, Tamil Nadu, India

[d]Department of Physics, Sri Krishnadevaraya University, Anantapur 515003, India

This journal is © The Royal Society of Chemistry 2025

J. Mater. Chem. A, 2025, **13**, 38039–38052 | **38039**

such as fly ash (FA) from the coal industry and ground granulated blast furnace slag (GGBS) from the steel industry. The elemental composition of FA and GGBS contains a trace amount of transition metal oxides such as Fe_2O_3, MgO, and TiO_2, which are essential for the faradaic redox reactions. Millions of tonnes of FA are generated globally due to coal combustion for power generation, with recent estimates indicating production of 750 million tonnes.[22] According to the World Steel Association, 1878 million tonnes of steel will have been produced by 2020. An estimated 300–360 million tonnes of GGBS are produced worldwide each year, with 100–150 kg produced for every tonne of molten steel and roughly 300 kg produced for each tonne of pig iron.[23] The disposal of this large amount of FA and GGBS is challenging and, therefore, it has become a serious environmental pollution issue. The utilization of industrial waste reduces the overall cost of the energy storage device.

Apart from the cost of supercapacitor devices, there are various other main components of a supercapacitor that require special attention, such as electrodes, electrolytes, current collectors, and separators.[24] The nature of the electrolyte material is a significant factor in the charge storing mechanism. Electrolytes also increase the moment of charge and balance between the electrodes in supercapacitors.[25] The elemental alignment in the active material and its contact with the electrolyte play a crucial role in determining the efficiency of charge transfer between the electrode and the electrolyte.[26] To develop a high-performance supercapacitor device, researchers have to carefully choose a suitable electrolyte solution. Supercapacitors commonly employ five types of electrolytes: organic, aqueous, ionic, solid-state, and redox electrolytes.[27] Aqueous-based electrolytes improve capacitance and conductance, but they are not widely used in commercial supercapacitors because of their limited potential range.[28,29] But organic electrolytes offer a much wider potential window, which is why commercially available supercapacitors use organic electrolytes instead of aqueous-based electrolytes. However, aqueous electrolytes are particularly favored in the laboratory because of their facilitating properties in the construction of supercapacitors, such as cost-effectiveness, ease of handling, abundance, and low ionic resistivity.[30] As they have a lower dynamic viscosity than solid and non-aqueous electrolytes, they typically exhibit higher conductivity. Aqueous electrolytes can be further classified into three types: alkaline or basic, acidic, and neutral.[27] Among these, the most commonly used aqueous electrolytes include potassium hydroxide (KOH), potassium chloride (KCl), sulfuric acid (H_2SO_4), sodium chloride (NaCl), nitric acid (NH_3), sodium hydroxide (NaOH), and sodium sulfate (Na_2SO_4).[31,32] So, in the current study, the effect of alkaline-based aqueous electrolytes on the electrochemical properties of industrial waste-based supercapacitors was thoroughly investigated. Apart from the nature of electrolytes, the electrolyte concentration also influences the electrochemical studies.[33] When the electrolyte concentration increases, ion transport within the electrode layer becomes more efficient, allowing the supercapacitor to work more effectively.[34] However, too high electrolyte concentrations can decrease the performance of supercapacitors because of less water hydration, which reduces the ion activity.[35]

In the present work, we therefore extend the investigation by employing different electrolytes (KOH, NaOH, and their combination) and subsequently varying the molar concentration of KOH from 1 M to 7 M. This work presents a cost-effective and eco-friendly approach for converting industrial waste materials into value-added products for clean energy generation and capacitive energy storage applications. The fabricated electrode showed superior electrochemical properties with a 3.0 M KOH electrolyte. In terms of the supercapacitor application, the prepared material in a three-electrode configuration presented a specific capacitance of 1590 F g^{-1} at a current density of 3 A g^{-1} using 3.0 M KOH electrolyte. Moreover, an attempt was made to fabricate the coin cell device (two electrode system) with Ni foam as a current collector with 3.0 M KOH electrolyte. The as-fabricated device showed a decent energy density of 10.66 Wh kg^{-1} and a power density of 660 W kg^{-1}. The results showed that the symmetrical coin cell device achieved a specific capacitance of 120 F g^{-1} and maintained excellent capacitance retention of 93% after 5000 cycles. Additionally, two-coin cells connected in series were able to power a red LED, a digital watch, and an electronic calculator.

2. Experimental section

2.1. Active material preparation

The active material was prepared using the sol–gel method of synthesis by taking industrial waste FA and GGBS as initial precursors. FA and GGBS were separately dissolved in an equal weight ratio with NaOH and HCl solutions. The list of chemicals used in the study, their purities, and suppliers are shown in S1 Table S1 in the SI file. Firstly, solution A was prepared by dissolving a stoichiometric amount of GGBS in the 2.0 M solution of HCl and stirring the complete mixture for 1 hour under normal ambient conditions. Secondly, solution B was prepared by dissolving FA in a stoichiometric amount of 2.0 M NaOH solution and stirring the mixture continuously for 1 hour at 80 °C. To get rid of any undissolved contaminants, solutions A and B were filtered separately using Whatman filter paper with a 6 mm pore size. Furthermore, both solutions were mixed dropwise with constant stirring to obtain a white sol mixture. To allow the white sol solution to become a gel, the solution was placed in a sealed container and stored at room temperature for three days. After that, a centrifuge machine was used to wash the gelled solution three to four times with deionized (DI) water to get rid of any remaining salts. After washing, the sample was dried at 80 °C overnight and further ground finely with a mortar and pestle to get the powder. The active material preparation procedure is depicted in Fig. 1, and the dry powder was subsequently calcined for three hours at 950 °C. The calcined sample was then utilized as the active material for the supercapacitor electrode and for characterisation.

2.2. Electrode preparation

For the electrode preparation, the amounts of active material, carbon black, and polyvinylidene fluoride (PVDF) were measured according to the 8 : 1 : 1 proportion, respectively, and all of them were ground using a mortar and pestle. A suitable
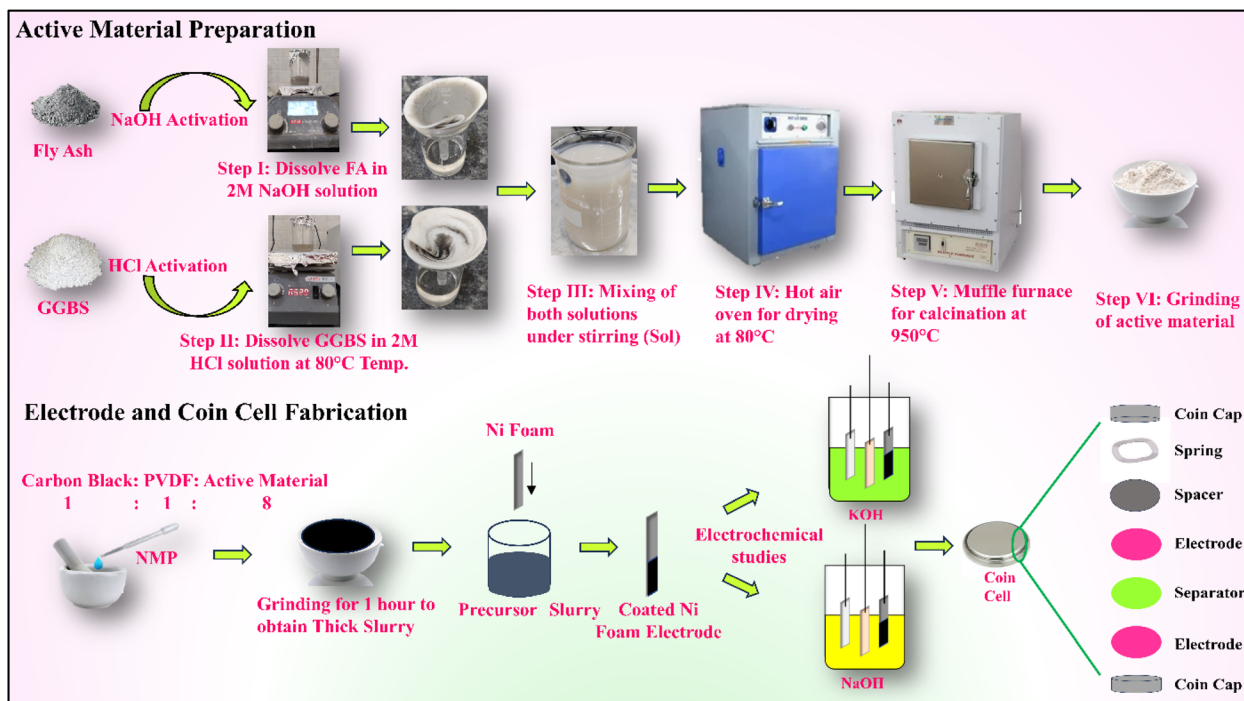
38040 | J. Mater. Chem. A, 2025, **13**, 38039–38052

This journal is © The Royal Society of Chemistry 2025

Fig. 1 Pictorial representation of the sol–gel method of synthesis of the active material and electrode.

amount of organic *N*-methyl-2-pyrrolidone (NMP) solvent was added to the mixture, which was then continuously ground for 1 hour to obtain a uniform, homogeneous slurry. Meanwhile, the current collector (nickel foam) was placed in the container of an ultrasonic cleaner to ensure the foam was clean and free from all contaminants that may hinder electrode adhesion or electrochemical performance. To clean the foam, the ultrasonic cleaner tank was filled with the prepared cleaning solution separately with ethanol, methanol, and 1.0 M HCl, ensuring that the nickel foam was fully submerged. The nickel foam was removed from the ultrasonic cleaner and given a good rinsing with distilled water when the cleaning cycle was finished. This stage aided in getting rid of all residual cleaning solutions from the foam. Then, the Ni foam was allowed to air dry in a hot air oven after washing. Furthermore, the prepared electrode slurry was applied onto the cleaned Ni foam substrate using the dip-coating technique, ensuring a uniform coverage of the substrate with the electrode slurry. Once the coating was applied, the electrode was dried at 80 °C in a hot air oven to remove the solvent and solidify the electrode film. The loading of the active material on the Ni foam substrate was determined by a gravimetric method using a high-precision analytical balance. The active material was uniformly loaded onto the current collector at a mass of 0.9 mg over an area of 1 cm × 1 cm by the dip coating technique. Details of the active material weight calculation are given in the SI file. Fig. 1 provides a visual representation of the electrode and the coin cell fabrication process.

The fabrication of the coin cell and its associated components is depicted in Fig. 1. The slurry was prepared by following the same composition ratio as in the three-electrode study, utilizing Ni foam as the current collector. Subsequently, a 3.0 M

KOH solution was prepared, and a few drops were applied to cellulose-based separators. The coin cell was then assembled by sandwiching the electrode with a spacer alongside other coin cell components.

The electrochemical characteristics of the synthesized material and a comparative analysis of the electrochemical behavior were investigated in diverse aqueous electrolytes. The different electrolytes, namely 1.0 M KOH, 1.0 M NaOH, 3.0 M KOH, 5.0 M KOH, 7.0 M KOH, 1.0 M KOH + 0.5 M NaOH, and 1.0 M NaOH + 0.5 M KOH, were prepared for testing. A three-electrode setup was used, with a platinum electrode as a counter electrode, Ag/AgCl acting as a reference electrode, and the working electrode consisting of an active material layer on nickel foam. In this study, various salts were used in the aqueous electrolyte, resulting in changes in electrical conductivity. This variation was primarily due to the specific behavior and interactions between the anions and cations of the salts. The solution's conductivity is influenced by the concentration of salt in the aqueous solvent. At lower concentrations of the electrolytic ions in the solution, the number of free ions is dominant, which enhances the ionic conductivity. However, at a very high concentration of ions, it can lead to strong associations between anions, cations, and neutral ions, which can diminish the number of free ions. In a high-viscosity ionic liquid system, conductivity usually declines monotonically as the concentration of the solution increases. This phenomenon is popularly known as the salt effect. So, mainly the delicate equilibrium between the free ion concentration and the viscosity of the solution can increase the electrochemical performance.

This journal is © The Royal Society of Chemistry 2025

J. Mater. Chem. A, 2025, **13**, 38039–38052 | **38041**

2.3. Characterization

The material characteristics were examined using a range of analytical techniques. Thermo-Gravimetric and Differential Thermal Analysis (TG-DTA) was performed using Holmarc HO-TH-OSC equipment to determine the sample's calcination temperature and weight loss in comparison with temperature. X-Ray Fluorescence (XRF) analysis was carried out using a ZSX Primus IV instrument to examine the elements' chemical composition. A PANalytical X'Pert Powder model X-ray diffractometer was used to perform X-ray Diffraction (XRD) analysis in order to determine the material's crystallinity. To determine the functional groups in the sample, Fourier Transform Infrared (FTIR) analysis using the KBr pellet technique on a Bruker TENSOR 27 spectrometer was carried out. An optical tensiometer was used to measure the contact angle of the electrolytes with the current collector. The Brunauer–Emmett–Teller (BET) analysis was carried out using a Quantachrome Autosorb iQ2 instrument to provide information on the material's porosity and specific surface area. The two-electrode and three-electrode electrochemical studies were performed with an Origalys Electrochem (OGF01A) instrument.

3. Results and discussion

3.1. Crystallographic analysis of the electrode materials

Thermo-Gravimetric and Differential Thermal Analysis (TG-DTA) of the dried powder revealed two significant weight losses: the first, around 14.8%, occurred between 30 °C and 280 °C due to dehydration; the second, approximately 7.13%, took place between 280 °C and 545 °C and was attributed to incomplete condensation (in SI S4 Fig. S1(a)). Furthermore, the stable mass was observed after 810 °C, with an exothermic peak on the DSC curve at 930 °C indicating crystallization of the prepared sample.

X-Ray Diffraction (XRD) analysis is an ideal method for assessing the crystallinity or amorphous nature of the sample intended for supercapacitor applications. In SI, S4 Fig. S1(b) shows the XRD patterns of akermanite ($Ca_2MgSi_2O_7$) powders prepared via the sol–gel synthesis process and calcined at 950 °C. The patterns exhibit a prominent akermanite peak at approximately 31.41° 2θ, confirming that the main phase is akermanite (JCPDS no: 35-0592). In addition to akermanite, a minor phase of diopside ($CaMgSi_2O_6$) is also present in the sample.[36] X-Ray Fluorescence (XRF) spectroscopy was conducted on the FA, GGBS, and the prepared sample to know the elemental composition (SI (S2 Table S2)). The results showed that FA is a rich source of SiO_2, while GGBS is rich in CaO. Additionally, trace metal oxides were detected in the prepared sample, which play a significant role in influencing its electrochemical properties. Furthermore, the prepared sample is characterized with X-ray Photoelectron Spectroscopy (XPS) analysis to check the presence of Fe, Ti, and Mg elements. The detail about the XPS study is shown in SI S6 Fig. S2.

3.2. Surface functional groups and Brunauer–Emmett–Teller (BET) analysis of akermanite

Fourier Transform Infrared (FTIR) spectra were recorded to confirm the phase composition of the powder. The FTIR spectra

of the prepared akermanite powder subsequent heat treatment at 950 °C are displayed in SI S4 Fig. S1(c). The O–Ca–O bending mode is confirmed by the band at 415 cm^{-1}, whereas the O–Mg–O bending mode is identified by the band at 486 cm^{-1}. O–Si–O vibrations are linked to the dual absorption bands at 640 cm^{-1} and 682 cm^{-1}, whereas Si–O stretching is linked to the band at 852 cm^{-1}. Additionally, symmetric Si–O–Si stretching is attributed to the 1024 cm^{-1} band. Fe–O is responsible for the vibration band at 528 cm^{-1}. These FTIR data showed a good correlation with the XRD findings.[37]

Additionally, as illustrated in S4 Fig. S1(d), the specific surface area and porosity of the sample were evaluated with the help of the nitrogen adsorption–desorption method following its calcination at 950 °C. The graph displays a type IV isotherm, which shows that multilayer adsorption occurs at higher pressures after a monolayer forms at low relative pressure. BET analysis confirmed the presence of a mesoporous structure,
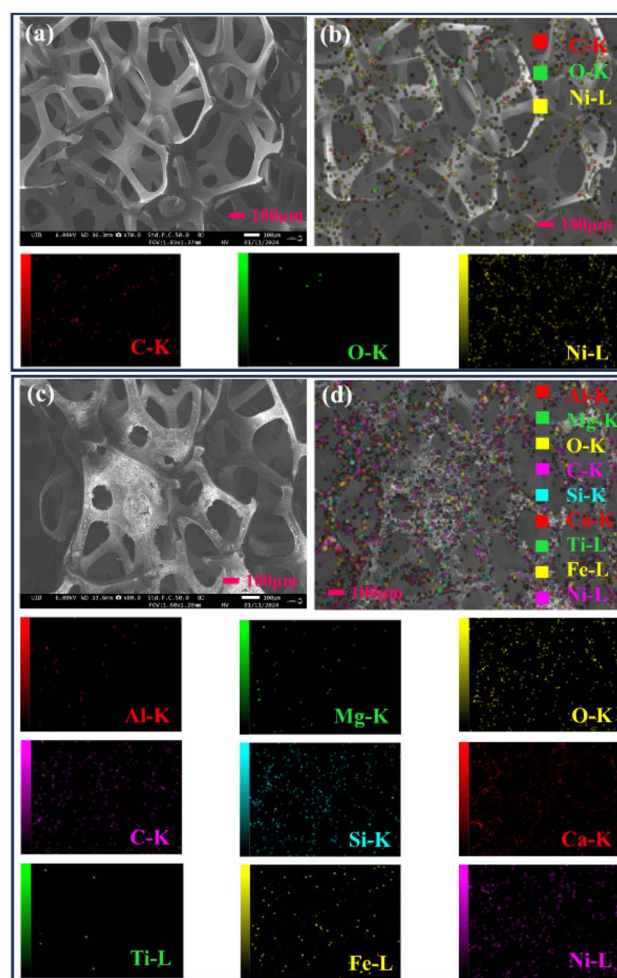

Fig. 2 (a) FE-SEM image of bare Ni foam; (b) top view of elemental mapping of the bare Ni foam showing carbon, oxygen, and nickel elements; (c) FE-SEM image of Ni foam coated with the active material prepared using fly ash and ground granulated blast furnace slag; (d) top view of elemental mapping of the coated Ni foam showing aluminum, magnesium, oxygen, carbon, silicon, calcium, titanium, iron and nickel elements.

38042 | J. Mater. Chem. A, 2025, 13, 38039–38052

This journal is © The Royal Society of Chemistry 2025

revealing a specific surface area of 89.25 m^2 g^{-1}.[38] For detailed studies about the prepared material properties, please refer to our previously published article.[38]

3.3. Field emission scanning electron microscopy (FE-SEM)

FESEM was employed to investigate the morphology and chemical composition of the prepared electrode, as shown in Fig. 2. The examination of bare nickel foam reveals a smooth, zigzag hollow structure. In contrast, FESEM images of material-coated on nickel foam show the growth of the material on the foam's surface. The analysis suggests that during the dip coating process, the original zigzag hollow structure of the Ni foam remains intact, and the material derived from industrial waste precursors uniformly and densely covers the foam. FESEM and energy-dispersive X-ray spectroscopy (EDX) elemental mapping further validates the presence of carbon (C), oxygen (O), and nickel (Ni) metals in the uncoated nickel foam, as depicted in Fig. 2(b). The elements present in coated-nickel foam are C, O, Ni, Ca, Si, Mg, Al, Fe, and Ti, as depicted in Fig. 2(d). This distinctive 3D architecture of the nickel foam with the material contributes to a high specific surface area and prevents the self-aggregation of active sites, facilitating efficient mass and charge transport to enhance electrocatalytic properties.[39]

4. Electrochemical studies

4.1. Cyclic voltammetry

Electrochemical testing of the sample was conducted in various aqueous electrolyte solutions, including 1.0 M NaOH, 1.0 M KOH, 3.0 M KOH, 5.0 M KOH, 7.0 M KOH, and binary mixtures such as 1.0 M NaOH + 0.5 M KOH and 1.0 M KOH + 0.5 M NaOH, at room temperature. In Fig. 3, the electrodes' cyclic

voltammetry (CV) curves in various electrolytic solutions are displayed at various scan rates between 10 and 100 mV s^{-1}. The mirrored redox peaks observed in the plot of each sample indicated the occurrence of faradaic reactions at the surface of the electrode. The possible reactions for the oxidation and reduction peaks in the CV analysis and detailed description are shown in eqn (S1)–(S5). This electrochemical behavior of the electrodes was attributed to trace amounts of transition metal ions in the material.[40] Notably, during the charging and discharging processes in alkaline electrolytes, two redox peaks on each CV plot were linked to the redox reactions (MO/MOOH, M = Mg, Fe, or Ti), demonstrating the pseudocapacitive behavior.[41] In the KOH and NaOH electrolytic solutions, the redox reaction involved OH$^-$ electrolyte ions.[42] At a scan rate of 10 mV s^{-1}, Fig. 3 shows that the material's CV curve showed duck-shaped characteristics, covering a greater area in the KOH electrolyte than in NaOH and a binary mixture of KOH and NaOH. The CV curves showed diverse areas corresponding to different electrolytes due to their different physical properties. Additionally, the following eqn (1)[43] was used to compute the specific capacitance based on the CV plot:

$$C_{sp} = \frac{\int_{V_1}^{V_2} i \times V \times dV}{m \times \nu \times (V_2 - V_1)} \tag{1}$$

where i is the corresponding current, m is the mass of the electroactive material, ν is the scan rate, and V_1 and V_2 are the two working potential limits.

The specific capacitance values obtained for 1.0 M KOH and 1.0 M NaOH at a scan rate of 10 mV s^{-1} are 1973 F g^{-1} and 1230 F g^{-1}, respectively. These findings indicate that a 1.0 M KOH electrolyte exhibits a higher specific capacitance than both a 1.0 M NaOH electrolyte and a binary mixture of NaOH and KOH electrolytes. This result is surprising, as the literature suggested
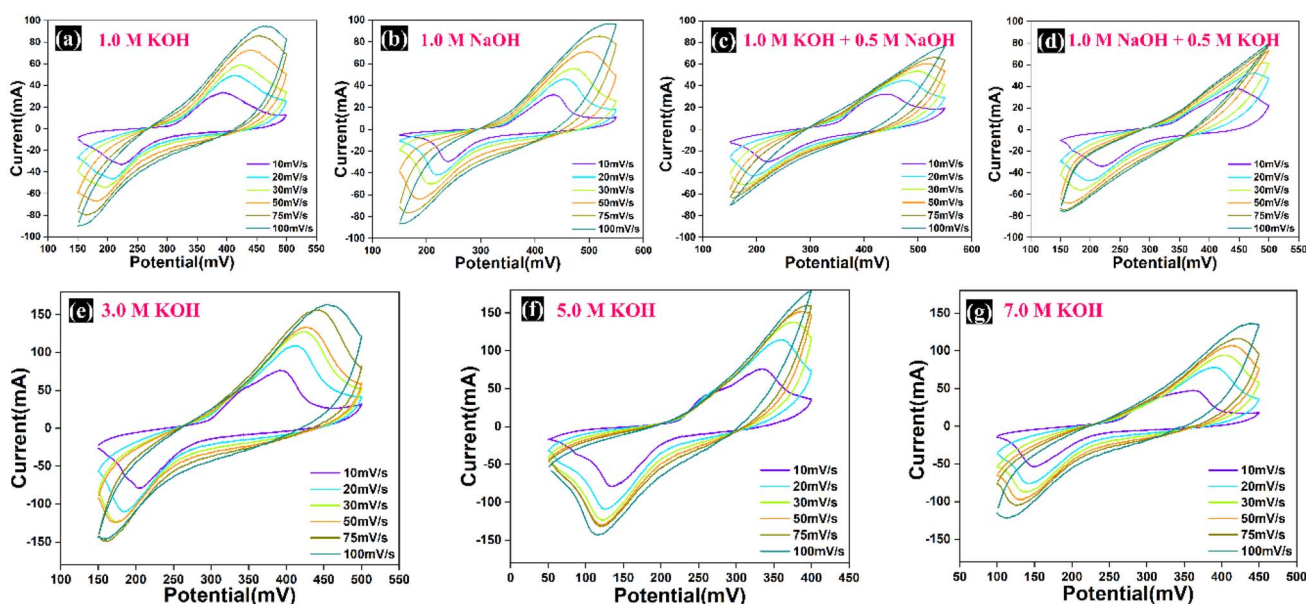

Fig. 3 Cyclic voltammetry curves of the prepared electrode with different electrolytic solutions: (a) 1.0 M KOH, (b) 1.0 M NaOH, (c) 1.0 M KOH + 0.5 M NaOH, (d) 1.0 M NaOH + 0.5 M KOH, (e) 3.0 M KOH, (f) 5.0 M KOH, and (g) 7.0 M KOH.

This journal is © The Royal Society of Chemistry 2025

J. Mater. Chem. A, 2025, **13**, 38039–38052 | **38043**

Table 1 Physical characteristics of aqueous electrolytes and their mixtures, including density, viscosity, contact angle, and conductivity

Electrolytes	Density (g cm^{-3})	Viscosity (cP)	Contact angle	Conductivity (mS cm^{-1})
1.0 M KOH	1.05	0.9569	17°	143.5
1.0 M NaOH	1.041	1.0000	26°	87.8
3.0 M KOH	1.14	1.1600	13°	146.2
5.0 M KOH	1.27	1.2400	20°	150.7
7.0 M KOH	1.32	1.3000	25°	159.0
1.0 M KOH + 0.5 M NaOH	1.035	1.9569	57°	90.2
1.0 M NaOH + 0.5 M KOH	1.025	1.9631	58°	75.3

that the NaOH electrolytes should have the highest specific capacitance due to the smaller ionic radius of Na$^+$ ions (0.95 Å) and their more efficient intercalation compared to K$^+$ ions (1.33 Å).[44] However, the observed results contradict this expectation, showing a specific capacitance ranking in the order of 1.0 M KOH > 1.0 M NaOH. This discrepancy can be explained by the behavior of the electrolyte's cations (Na$^+$ and K$^+$) in aqueous solutions.

In the aqueous solution, smaller ionic radii ions usually form bigger hydrated radii ions and *vice versa*. In contrast to K$^+$ ions, which form smaller hydrated ions with a radius of 3.31 Å, Na$^+$ ions make larger hydrated ions with a radius of 3.58 Å. This difference in hydrated ionic sizes explains the observed rise in specific capacitance when using a 1.0 M KOH electrolyte instead of a 1.0 M NaOH electrolyte.[45,46] To determine rate capability, cyclic voltammetry (CV) tests were performed at increasing scan rates. Fig. 3 shows the CV curves at different scan rates (10–100 mV s^{-1}) for all electrolytes, revealing an expanding area under the CV curve with increasing scan rate, indicative of strong rate capability. The obtained values show that specific capacitance steadily decreases with increasing scan rate, as the diffusion time for ions in the active material decreases.

After these observations, the findings made us curious about how combining different electrolytes might affect the specific capacitance of the material. Consequently, binary solutions were formulated to enhance the understanding of electrolyte behavior and its impact on the performance of the supercapacitor. The CV curves, as shown in Fig. 3(c and d), display faradaic redox peaks that closely resemble those of individual aqueous electrolytes. The specific capacitance for the electrolyte solutions 1.0 M KOH + 0.5 M NaOH and 1.0 M NaOH + 0.5 M KOH was found to be 1243 F g^{-1} and 1221 F g^{-1}, respectively, at a 10 mV s^{-1} scan rate. It was anticipated that the specific capacitance of a combined electrolyte solution would be the average of the individual electrolyte capacitances.[47] This expectation prompted an investigation into other physical properties that might influence the electrochemical properties when using a mixture of electrolytes. Table 1 presents various physical properties, including density, viscosity, contact angle, and conductivity, which were measured and compared for each electrolyte to identify potential correlations. Notably, the conductivity values for 1.0 M KOH, 1.0 M NaOH, 3.0 M KOH, 5.0 M KOH, 7.0 M KOH, 1.0 M KOH + 0.5 M NaOH, and 1.0 M NaOH + 0.5 M KOH electrolytes were observed to be 143.5, 87.8, 146.2, 150.7, 159.0, 90.2, and 75.3 mS cm^{-1}, respectively.

The contact angle measurement data indicated the existence of a porous network in the material-coated Ni foam, allowing the complete adsorption of a 3.0 M KOH liquid droplet within the pore space, showcasing super hydrophilicity on the surface (contact angle = 13°). This observation reinforces the notion that K$^+$ ions originating from KOH electrolytes undergo adsorption, resulting in the formation of smaller hydrated ions that effectively facilitate ion intercalation within the pores of the coated Ni foam. In contrast, NaOH impedes intercalation by generating larger hydrated ions. This phenomenon is attributed to the alteration in surface–interface properties of electrodes in the presence of different aqueous electrolytes.[48] So, the smaller the contact angle, the greater the adsorption of electrolytic species, which enhances the performance of the electrode.[49] Furthermore, to investigate the effect of molarity, the cyclic voltammetry (CV) curves for the electrode were observed in 3.0 M, 5.0 M, and 7.0 M KOH electrolytes at a scan rate ranging from 10 to 100 mV s^{-1} within the potential window of 0.15–0.5 V, as displayed in Fig. 3(e–g). The analysis of the current response and the area under the curve of the CV profile reveals that the 3.0 M KOH electrolyte solution exhibits notably favorable properties. The CV curves indicate a swift current response that increases from 1.0 M to 3.0 M KOH electrolyte and then decreases at 5.0 M and 7.0 M. By taking into account the size and mobility of the hydrated K$^+$ ions, this tendency can be explained. The size of the hydrated K$^+$ ions reduces with increasing KOH electrolyte concentration. At lower concentrations of KOH electrolyte, the larger size of hydrated K$^+$ ions creates obstacles for their entry and diffusion into the electrode, leading to a lower ion transport rate, this, in turn, diminishes the electrode's capacity. In consequence of this, smaller hydrated K$^+$ ions can more readily intercalate into the electrode during redox reactions at greater KOH concentrations, promoting rapid charge transfer and improving electrochemical performance.[50,51] In contrast, at 5.0 M and 7.0 M KOH electrolyte concentrations, the current density values decrease proportionally due to excessively high salt concentrations. Ionic mobility and the availability of free ions are decreased as a result of the cations and anions forming strong interactions with aqueous molecules. During electrochemical reactions, this leads to a decrease in specific capacitance and poor electrolyte conductivity. Furthermore, under conditions of higher concentration, all KOH ions accumulate on the surface of the electrode, resulting in increased internal resistance and

38044 | *J. Mater. Chem. A*, 2025, **13**, 38039–38052

This journal is © The Royal Society of Chemistry 2025

a decrease in ion activity, which in turn causes a decrease in current response.

In order to determine the qualitative impact of different electrode charge storage kinetics and processes, the power law equation was utilized, given in eqn (2).[43]

$$i = av^b \qquad (2)$$

In this equation, a and b are constants, i represents the current (in amperes), and v is the scan rate (in volts per second).

The b value varies between 0.5 and 1; when b is 0.5, it indicates a reaction controlled by semi-infinite diffusion, resembling battery-type behavior. In contrast, b being 1 signifies a reaction controlled by surface processes or electrosorption.[52] Fig. 4(a and b) shows the slopes (b values) obtained from $\log(i)$
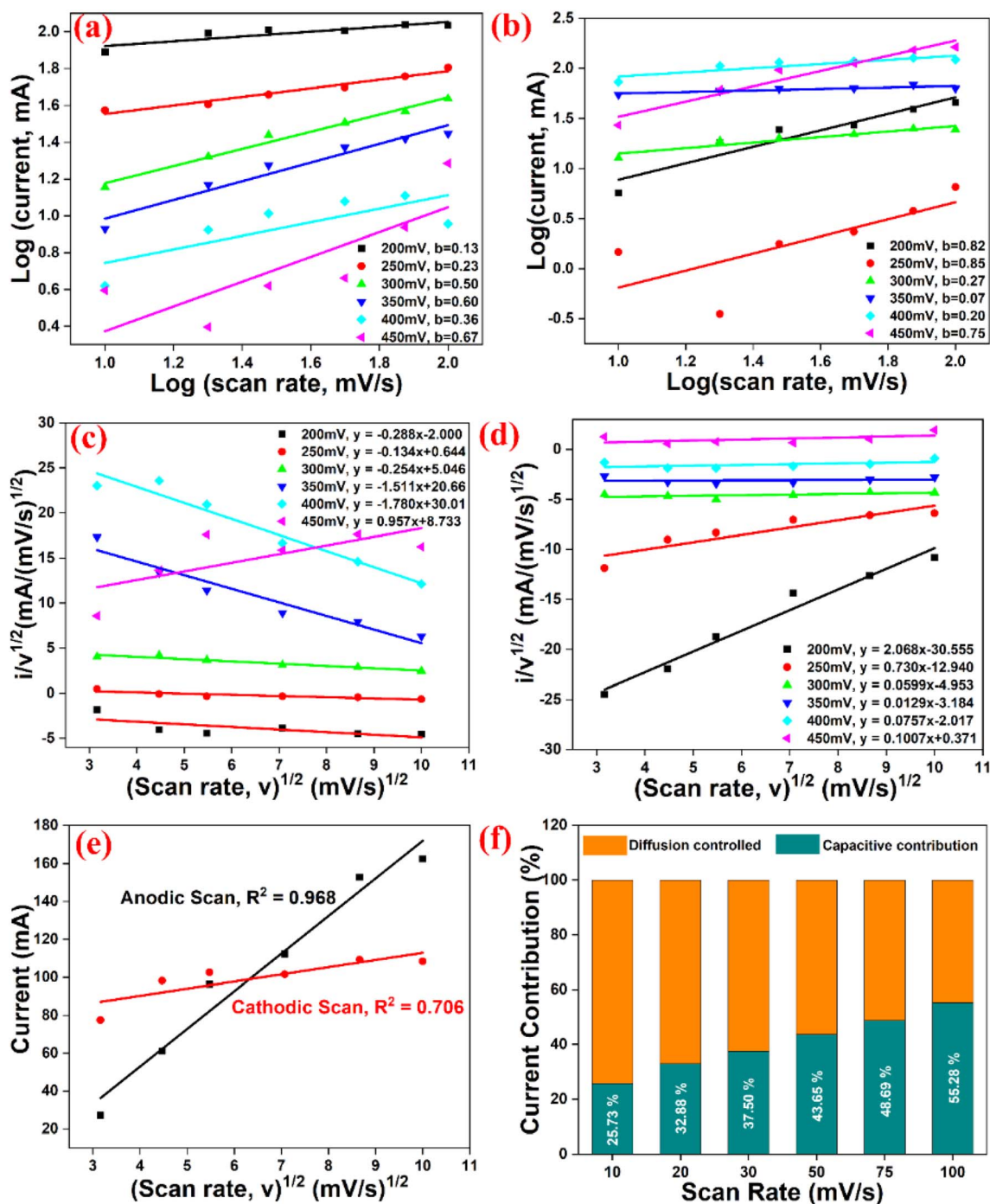
Fig. 4   (a) Log(peak current) *vs.* log(scan rate) for *b*-value calculation of the cathodic region; (b) log(peak current) *vs.* log(scan rate) for *b*-value calculation of the anodic region; (c) *k* values calculation for the anodic scan; (d) *k* value calculation for the cathodic scan; (e) *R* square calculation for the anodic and cathodic scans; (f) bar graph of the capacitive and diffusion-controlled contribution of material at various scan rates in 3.0 M KOH electrolyte.
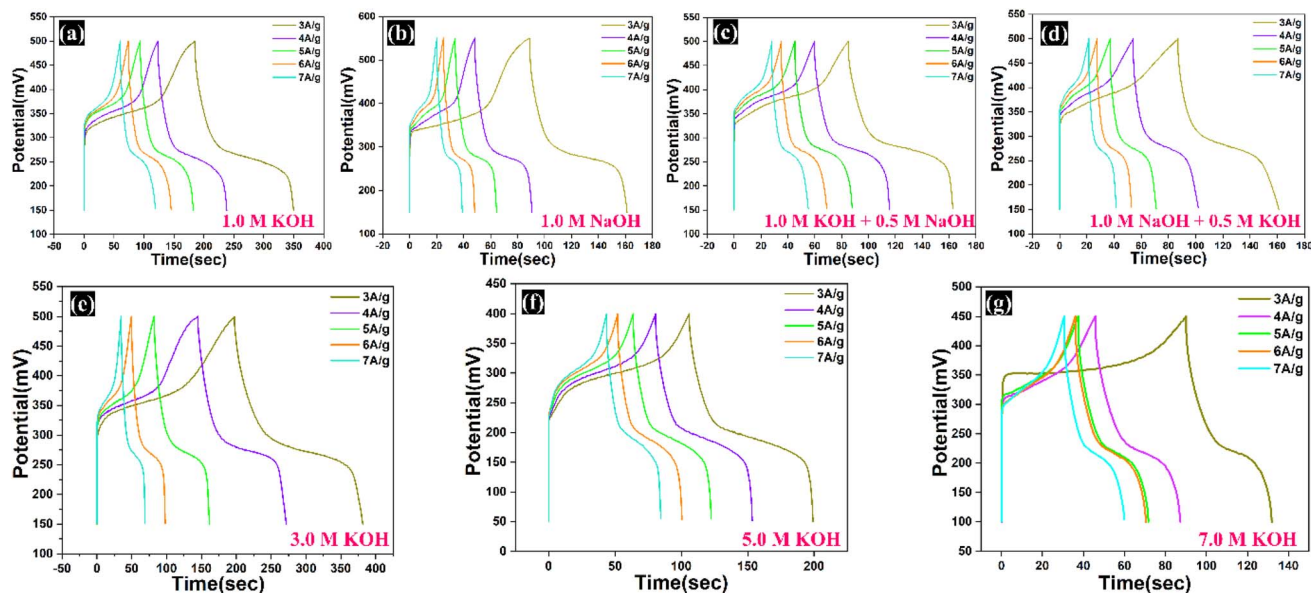
This journal is © The Royal Society of Chemistry 2025

J. Mater. Chem. A, 2025, **13**, 38039–38052 | **38045**

Fig. 5 Galvanostatic charge discharge curves of the prepared electrode with different electrolytic solutions: (a) 1.0 M KOH, (b) 1.0 M NaOH, (c) 1.0 M KOH + 0.5 M NaOH, (d) 1.0 M NaOH + 0.5 M KOH, (e) 3.0 M KOH, (f) 5.0 M KOH, and (g) 7.0 M KOH.

versus log(ν) plots. The *b*-values for the oxidative and reductive currents in Fig. 4(a and b) are primarily near 0.5, indicating the predominance of semi-infinite diffusion-controlled intercalative processes and implying behavior during the electrochemical reaction that is comparable to a battery-type supercapacitor. The figure also demonstrates the impact of varying the sweep rate in voltammetry, allowing for a quantitative distinction between the capacitive contribution and the combined effects of surface capacitance and diffusion-controlled insertion or intercalation on the current response at a fixed potential.

The overall current is measured at a specific potential (V) and is a combination of two components: charge storage due to capacitive processes (independent of diffusion) and charge storage *via* diffusion-controlled intercalation. Eqn (3) quantifies this relationship, where $k_1\nu$ represents the capacitive current contribution and $k_2\nu^{0.5}$ represents the diffusion-controlled current contribution.[53]

$$i(V) = k_1\nu + k_2\nu^{0.5} \quad (3)$$

The slope (k_1) and intercept (k_2) of the plot of eqn (3) are used to identify the capacitive and diffusion behavior. Fig. 4(c and d) shows the representative curve ($i(V)/\nu^{0.5}$ *vs.* $\nu^{0.5}$), which highlights the effects of surface capacitance and diffusion-controlled intercalation at various scan rates. Fig. 4(f) identifies the specific contributions at a 10 mV s^{-1} scan rate, with surface capacitance or electrosorption accounting for 25.73% and diffusion-controlled intercalation contributing approximately 74.27%. The diffusion and capacitive capacitance contribution at various scan rates from 10 mV s^{-1} to 100 mV s^{-1} is shown in the SI S7 Fig. S3. Furthermore, Fig. 4(e) displays a plot of current against the square root of scan rate ($\nu^{1/2}$), with correlation

coefficients (R^2) of 0.706 and 0.968, suggesting an adsorption-controlled electrode process.

4.2. Galvanostatic charge–discharge analysis

GCD tests were performed to assess the supercapacitor performance of different electrolytes and their combinations at current densities ranging from 3 A g^{-1} to 7 A g^{-1}. The results of these tests are presented in Fig. 5. The pseudocapacitive behavior of the electrode material is indicated by the nonlinearity seen in the GCD plots, which is consistent with the findings of the CV test. Eqn (4)[43] is used to determine the specific capacitance derived from the GCD curves, taking the discharge time into account:where

$$C_{sp} = \frac{i \times t}{\Delta V \times m} \quad (4)$$

t, ΔV, and i represent the discharge duration (s), potential window (V), and current density (A g^{-1}), respectively. At a constant current density of 3 A g^{-1}, the highest specific capacitance values were found to be 1410 F g^{-1} for 1.0 M KOH, 555 F g^{-1} for 1.0 M NaOH, 668 F g^{-1} for 1.0 M KOH + 0.5 M NaOH, and 547 F g^{-1} for 1.0 M NaOH + 0.5 M KOH electrolytes. The discharge at 3 A g^{-1} demonstrated extended discharge times for the KOH electrolyte compared to NaOH and the mixture of KOH and NaOH. The observed asymmetry in discharge curves suggests faradaic reactions at the electrode surface, potentially attributed to oxygen-containing functional groups on both the Ni-foam and the coated material.

The GCD performances of the electrode were investigated at current densities ranging from 3 A g^{-1} to 7 A g^{-1} for 3.0 M, 5.0 M, and 7.0 M KOH electrolyte concentrations, as shown in Fig. 5(e–g). The GCD curves show a non-symmetric profile consisting of two separate regions: a long, flat plateau followed
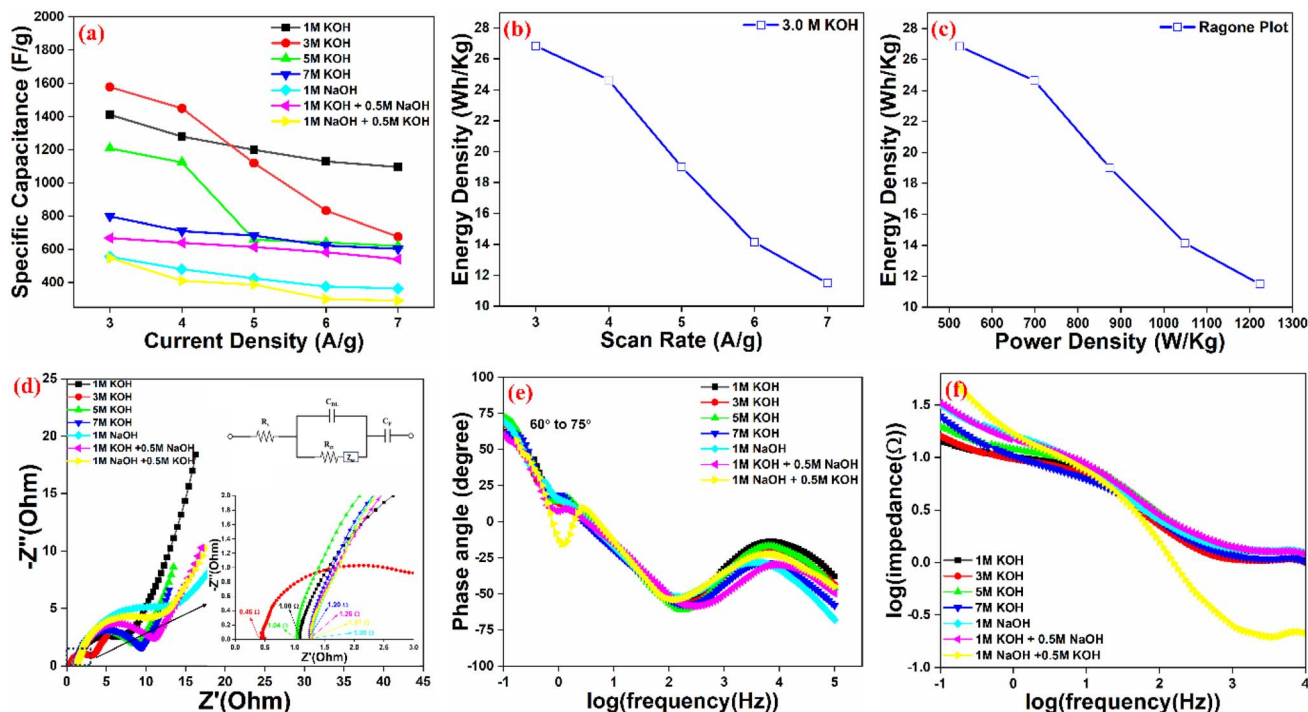
38046 | *J. Mater. Chem. A*, 2025, **13**, 38039–38052

This journal is © The Royal Society of Chemistry 2025

Fig. 6 (a) Specific capacitance as a function of different scan rates for different electrolytes, (b) change of energy density with current density, (c) Ragone plot, (d) Nyquist plot of the material in various electrolytes, (e) Bode phase angle profiles of the materials analyzed in different electrolytes, and (f) log impedance plotted against log frequency graph.

by an abrupt voltage decrease. These characteristics point to a quasi-faradaic redox mechanism, suggesting that the electrode exhibits battery-like charge storage characteristics.[54] The charge–discharge duration increases proportionately within the concentration range of 1.0 M to 3.0 M KOH, according to an analysis of the GCD curves. The charge–discharge time, however, reduces with higher electrolyte concentrations of 5.0 M and 7.0 M KOH. Similar to the CV analysis, this behavior is related to the size and ionic mobility of the hydrated K^+ ions. Additionally, the coulombic efficiency (η) of the electrode is calculated to be 0.93 using eqn (5).

$$\eta = \frac{t_d}{t_c} \tag{5}$$

The charging time is denoted by t_c and the discharging time by t_d. The shift of the calculated specific capacitance for various electrolytes with varying scan speeds is displayed in Fig. 6(a). The results indicate that the 3.0 M KOH electrolyte exhibits the highest specific capacitance at lower scan rates. Fig. 6(b) displays the electrode's energy density as a function of current density. Furthermore, the energy and power densities for the prepared electrode were determined using eqn (6) and (7),[43] respectively.

$$E\left(\text{Wh kg}^{-1}\right) = \frac{1}{2}C_s(\Delta V)^2 \times \frac{1000}{3600} \tag{6}$$

$$P\left(\text{W kg}^{-1}\right) = \frac{E}{t_d} \times 3600 \tag{7}$$

At current densities of 3 A g^{-1}, 4 A g^{-1}, 5 A g^{-1}, 6 A g^{-1}, and 7 A g^{-1}, respectively, the 3.0 M KOH electrolyte showed excellent energy density performance, obtaining values of 26.84 Wh kg^{-1}, 24.63 Wh kg^{-1}, 19.01 Wh kg^{-1}, 14.14 Wh kg^{-1}, and 11.48 Wh kg^{-1}. Interestingly, Fig. 6(c) shows that the supercapacitor using 3.0 M KOH electrolyte demonstrated an incredible energy density of 24.5 Wh kg^{-1} at a power density of 525 W kg^{-1}.

4.3. Electrochemical impedance spectroscopy

Electrodes in different electrolytes were subjected to Electrochemical Impedance Spectroscopy (EIS) at frequencies ranging from 100 kHz to 0.1 Hz. The Nyquist plot in Fig. 6(d) illustrates the typical capacitive behavior, which is a half semicircle in the high-frequency range and a nearly vertical line in the low-frequency range. The 1.0 M NaOH electrolyte showed an indistinct Warburg diffusion line at low frequencies and a larger semi-circle at high frequencies, which corresponded to a greater R_{ct} value. In contrast, the 3.0 M KOH electrolyte exhibited smaller semi-circles at higher frequencies, indicative of lower R_{ct} values and hence enhanced electron transfer kinetics at the interface of the electrode and electrolyte.[34] The R_{ct} values for other electrolyte solutions fall between those observed for 1.0 M NaOH and 3.0 M KOH. Additionally, all compositions display a Warburg diffusion line at low frequency, with 3.0 M KOH exhibiting a more pronounced Warburg line. The nearly parallel orientation of the Warburg line to the imaginary impedance axis in 3.0 M KOH suggests a more pseudocapacitive behavior. The lower Z_W values indicate more

Table 2 Comparison with the recently published literature

S. no.	Electrode material	Current collector	Electrolyte	Specific capacitance (F g^{-1})	Ref.
1	Activated carbon from lignocellulose-based bio-waste	Ni foam	2.0 M KOH	565.2 F g^{-1} @ 0.5 A g^{-1}	56
2	Porous carbon derived from animal bone	Ni foam	4.0 M Al(No$_3$)$_3$	804 F g^{-1} @ 1 A g^{-1}	4
3	Porous carbon from marine biowaste	—	Choline chloride based deep eutectic	657 F g^{-1} @ 1 A g^{-1}	57
4	Carbonized jute fibers from jute rope	Ni foam	3.0 M KOH	185 F g^{-1} @ 0.5 A g^{-1}	6
5	Activated carbon from peanut (*Arachis hypogaea*) shell waste	Nickel foil	6.0 M KOH	290 F g^{-1} @ 0.2 A g^{-1}	58
6	Porous biocarbon from konjaku flour	KOH and Na$_2$SO$_4$ aqueous electrolyte	6.0 M KOH	533 F g^{-1} @ 0.5 A g^{-1}	59
7	Akermanite derived from industrial waste	Ni foam	3.0 M KOH	1590 F g^{-1} @ 3 A g^{-1}	This Work

effective capacitive kinetics in charge storage, whereas a more vertical curve shows that the supercapacitor (or pseudo-capacitor) acts more like an ideal capacitor.[55] An enlarged view of the high-frequency area is displayed in Fig. 6(d) inset, which also highlights the R_s values of electrodes treated with various electrolytic solutions. The inset of Fig. 6(d) illustrates how the EC-Lab EIS Z-fit program fits EIS data using an equivalent circuit model. From 1.0 M NaOH, 1.0 M NaOH + 0.5 M KOH, 1.0 M KOH + 0.5 M NaOH, 7.0 M KOH, 5.0 M KOH, and 1.0 M KOH to 3.0 M KOH, the R_{ct} and R_s values show a decrease in the trend. The R_s, C_{dl}, R_{ct}, Z_W, and C_F values through fitting of the experimental impedance spectra based upon the proposed equivalent circuit are 0.46 Ω, 3.2 Ω, 0.18 F g^{-1}, 110 F g^{-1}, and 0.11 MMho, respectively, for 3 M KOH electrolyte.

Fig. 6(e) presents the Bode plots for electrodes in different electrolytes. The electrode in 3.0 M KOH exhibits the highest phase angle, approaching the ideal capacitive behavior of 90°. This indicates a more pronounced pseudocapacitive nature compared to other electrolytes. The log impedance *versus* log frequency plots in Fig. 6(f) reveal lower impedance values for electrodes in 3.0 M KOH. This is further corroborated by the faster angular frequency response of the 3.0 M KOH material, suggesting more efficient ion transport pathways. The performance of the electrode is also compared with the recently published literature in Table 2.
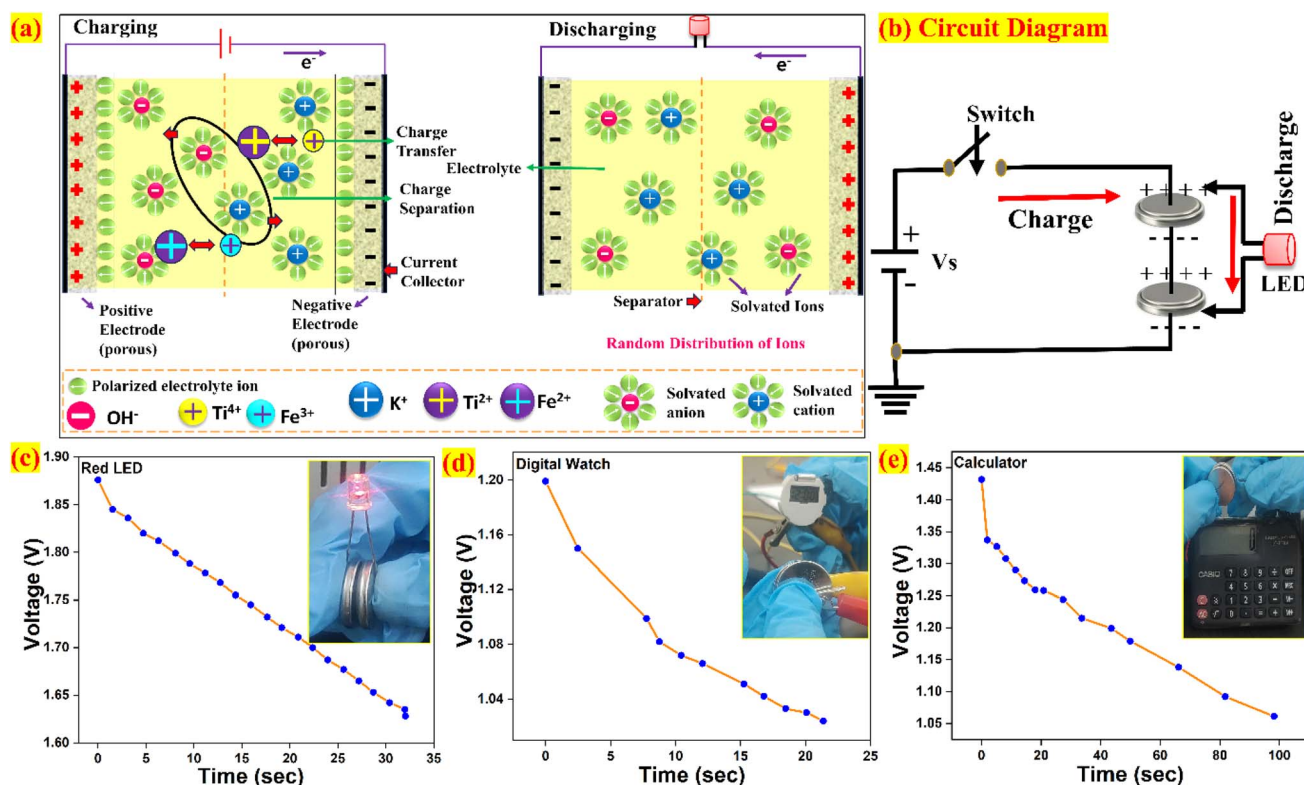

Fig. 7 (a) Charge–discharge mechanism of the electrode material with KOH electrolyte; (b) circuit diagram of charging and discharging of the device; (c–e) glowing of the LED, digital watch, and electronic calculator through the fabricated coin cell device.

38048 | *J. Mater. Chem. A*, 2025, **13**, 38039–38052

This journal is © The Royal Society of Chemistry 2025

4.4. Coin cell device

Extensive electrochemical studies were conducted on the assembled coin cell, including CV, GCD, and EIS measurements, all performed within a voltage range of 0 to 0.8 V. The device demonstrated exceptional reversibility, as evidenced by the quasi-rectangular shape of the curves consistently maintained at a high scan rate of 100 mV s^{-1}, as shown in S8 Fig. S4(a). In the SI, S8 Fig. S4(b) shows discharge characteristics curves with varying current densities of the device from 1 A g^{-1} to 5 A g^{-1}. The EIS analysis of the device in S8 Fig. S4(d) confirms the low resistivity. The assembled symmetric coin cell in a 3.0 M KOH electrolyte exhibited a specific capacitance of 120 F g^{-1}. Here, the capacitance is calculated based on the total active mass of both electrodes, which lowers the specific capacitance per gram. Being a practical device, it also incorporates internal resistance from both electrodes and the separator, leading to additional IR loss and reduced apparent capacitance. Furthermore, charge balancing between the two electrodes is required, and any imbalance in charge limits the overall device performance. Thus, several factors collectively contribute to the lower capacitance observed in the coin-cell system.[60] Furthermore, in S8 Fig. S4(c) illustrates the capacity retention of the fabricated coin-cell supercapacitor device. Cycling stability was evaluated over 5000 charge–discharge cycles using GCD studies. The device retained 97% of its capacity during the initial 1000 cycles, attributed to the activation process. Subsequently, there was a 4% decrease in capacity retention, maintaining 93% retention up to 4000 cycles. Beyond 4000 cycles, minimal particles were observed peeling off from the Ni foam, indicating slow degradation of the electrodes. The coin cell demonstrated a high power density of 660 W kg^{-1} and an energy density of 10.66 Wh kg^{-1}. Fig. 7(a) illustrates the suggested mechanism for the electrochemical supercapacitor cell's reaction. The electrochemical behaviour is exhibited because of the trace metal oxides present in the sample, such as TiO_2 and Fe_2O_3. Furthermore, an attempt is made to glow the electronic devices such as a red LED, a digital watch and a scientific calculator with the help of the circuit diagram shown in Fig. 7(b). Initially, the two-coin cells in series were charged using a 5 V DC power supply and further discharged through the devices. The calculator, LED, and clock were charged with a 5 V DC power supply for 25 seconds, 15 seconds, and 25 seconds, respectively, and then glowed for 110 seconds, 30 seconds, and 25 seconds, respectively. The voltage *versus* time graph of all three electronic gadgets is shown in Fig. 7(c–e). The coin cell device demo videos, enabling two cells in series to power a red LED (S4 V1), a digital watch (S5 V2), and an electronic calculator (S6 V3), are also submitted along with the manuscript.

5. Conclusion

The present study focused on synthesizing an active material from industrial waste to evaluate its potential for supercapacitor applications. The ultimate goal is to develop a material that is cost-effective, environmentally friendly, and produced through a simple synthesis process. The prepared sample exhibits an akermanite material with a surface area of 89.25 m^2 g^{-1}, demonstrating a mesoporous structure. A 3.0 M KOH electrolyte is appropriate, according to a thorough analysis of the material's electrochemical performance in a three-electrode system. This results in a high specific capacitance of 1590 F g^{-1} at a current density of 3 A g^{-1}. At a power density of 525 W kg^{-1}, the material demonstrated an excellent energy density of 24.5 Wh kg^{-1}. Apart from the electrode development, the recovery of stored energy in a coin cell supercapacitor using an integrated power electronic booster was demonstrated. The material demonstrated exceptional capacitance retention of 93% after 5000 cycles when tested in a real-time coin cell supercapacitor system. Additionally, the coin cell demonstrated a high power density of 660 W kg^{-1} and an energy density of 10.66 Wh kg^{-1}. The calculator, LED, and clock were charged with a 5 V DC power supply for 25 seconds, 15 seconds, and 25 seconds, respectively, and then glowed for 110 seconds, 30 seconds, and 25 seconds, respectively. By powering an LED, a digital watch, and an electronic calculator, the power electronic boost converter effectively raised the voltage as a proof of concept, enabling the recovery of stored energy. In summary, the symmetric coin cell's electrochemical performance in aqueous electrolytes indicates encouraging potential for use in energy storage devices.

Conflicts of interest

There are no conflicts to declare.

Data availability

The data supporting this article have been included as part of the supplementary information (SI). Supplementary information is available. See DOI: **https://doi.org/10.1039/d5ta06070b**.

Acknowledgements

References

1 D. S. Priya, L. J. Kennedy and G. T. Anand, Emerging Trends in Biomass-Derived Porous Carbon Materials for Energy Storage Application: A Critical Review, *Mater. Today Sustain.*, 2023, **21**, 100320, DOI: **10.1016/J.MTSUST.2023.100320**.

2 P. J. Megía, A. J. Vizcaíno, J. A. Calles and A. Carrero, Hydrogen Production Technologies: From Fossil Fuels toward Renewable Sources. A Mini Review, *Energy Fuels*, 2021, **35**(20), 16403–16415, DOI: **10.1021/acs.energyfuels.1c02501**.

3 S. Sundriyal, V. Shrivastav, H. D. Pham, S. Mishra, A. Deep and D. P. Dubal, Advances in Bio-Waste Derived Activated

This journal is © The Royal Society of Chemistry 2025

J. Mater. Chem. A, 2025, **13**, 38039–38052 | **38049**

Carbon for Supercapacitors: Trends, Challenges and Prospective, *Resour. Conserv. Recycl.*, 2021, **169**, 105548, DOI: 10.1016/j.resconrec.2021.105548.

4 Y. Al Haj, S. Mousavihashemi, D. Robertson, M. Borghei, T. Pääkkönen, O. J. Rojas, E. Kontturi, T. Kallio and J. Vapaavuori, Biowaste-Derived Electrode and Electrolyte Materials for Flexible Supercapacitors, *Chem. Eng. J.*, 2022, **435**, 135058, DOI: 10.1016/j.cej.2022.135058.

5 D. A and G. Hegde, Activated Carbon Nanospheres Derived from Bio-Waste Materials for Supercapacitor Applications – a Review, *RSC Adv.*, 2015, **5**(107), 88339–88352, DOI: 10.1039/C5RA19392C.

6 C. Zequine, C. K. Ranaweera, Z. Wang, P. R. Dvornic, P. K. Kahol, S. Singh, P. Tripathi, O. N. Srivastava, S. Singh, B. K. Gupta, G. Gupta and R. K. Gupta, High-Performance Flexible Supercapacitors Obtained via Recycled Jute: Bio-Waste to Energy Storage Approach, *Sci. Rep.*, 2017, **7**(1), 1174, DOI: 10.1038/s41598-017-01319-w.

7 Q. Hassan, S. Algburi, A. Z. Sameen, H. M. Salman and M. Jaszczur, A Review of Hybrid Renewable Energy Systems: Solar and Wind-Powered Solutions: Challenges, Opportunities, and Policy Implications, *Results Eng.*, 2023, **20**, 101621, DOI: 10.1016/j.rineng.2023.101621.

8 G. Kothandam, G. Singh, X. Guan, J. M. Lee, K. Ramadass, S. Joseph, M. Benzigar, A. Karakoti, J. Yi, P. Kumar and A. Vinu, Recent Advances in Carbon-Based Electrodes for Energy Storage and Conversion, *Adv. Sci.*, 2023, **10**(18), 2301045, DOI: 10.1002/advs.202301045.

9 M. A. Raza, U. Latif, A. Fazal, H. U. Rehman, S. M. S. Bukhari, M. Eriksson, M. J. Iqbal, S. Ali and B. S. Almutairi, Synthesis and Characterization of Zinc Aluminate Electrodes for Supercapacitor Applications, *Electrochim. Acta*, 2024, **475**, 143501, DOI: 10.1016/j.electacta.2023.143501.

10 L. M. Da Silva, R. Cesar, C. M. R. Moreira, J. H. M. Santos, L. G. De Souza, B. M. Pires, R. Vicentini, W. Nunes and H. Zanin, Reviewing the Fundamentals of Supercapacitors and the Difficulties Involving the Analysis of the Electrochemical Findings Obtained for Porous Electrode Materials, *Energy Storage Mater.*, 2020, **27**, 555–590, DOI: 10.1016/j.ensm.2019.12.015.

11 S. Huang, X. Zhu, S. Sarkar and Y. Zhao, Challenges and Opportunities for Supercapacitors, *APL Mater.*, 2019, **7**(10), 100901, DOI: 10.1063/1.5116146.

12 X. You, M. Misra, S. Gregori and A. K. Mohanty, Preparation of an Electric Double Layer Capacitor (EDLC) Using Miscanthus-Derived Biocarbon, *ACS Sustain. Chem. Eng.*, 2018, **6**(1), 318–324, DOI: 10.1021/acssuschemeng.7b02563.

13 S. B. Aziz, M. H. Hamsan, M. A. Brza, M. F. Z. Kadir and R. T. Abdulwahid, Fabrication of Energy Storage EDLC Device Based on CS : PEO Polymer Blend Electrolytes with High Li + Ion Transference Number Results in Physics Fabrication of Energy Storage EDLC Device Based on CS : PEO Polymer Blend Electrolytes with High Li + Ion Tran, *Results Phys.*, 2019, **15**, 102584, DOI: 10.1016/j.rinp.2019.102584.

14 X. You, M. Misra, S. Gregori and A. K. Mohanty, Preparation of an Electric Double Layer Capacitor (EDLC) Using Miscanthus -Derived Biocarbon, *ACS Sustain. Chem. Eng.*, 2018, **6**(1), 318–324, DOI: 10.1021/acssuschemeng.7b02563.

15 U. Latif, Z. U. Rehman, M. F. Maqsood, M. A. Raza, S. Ali, M. J. Iqbal, S. M. Z. Mehdi and N. Lee, In Situ Growth of Nickel Ammonium Phosphate Ribbons on Nickel Foam for Supercapacitor Applications, *J. Energy Storage*, 2023, **73**, 109024, DOI: 10.1016/j.est.2023.109024.

16 P. Sundriyal and S. Bhattacharya, Inkjet-Printed Electrodes on A4 Paper Substrates for Low-Cost, Disposable, and Flexible Asymmetric Supercapacitors, *ACS Appl. Mater. Interfaces*, 2017, **9**(44), 38507–38521, DOI: 10.1021/acsami.7b11262.

17 P. Kiddee, R. Naidu and M. H. Wong, Electronic Waste Management Approaches: An Overview, *Waste Manag.*, 2013, **33**(5), 1237–1250, DOI: 10.1016/j.wasman.2013.01.006.

18 R. A. Geioushy, S. Y. Attia, S. G. Mohamed, H. Li and O. A. Fouad, High-Performance Electrode Materials for Supercapacitor Applications Using Ni-Catalyzed Carbon Nanostructures Derived from Biomass Waste Materials, *J. Energy Storage*, 2022, **48**, 104034, DOI: 10.1016/j.est.2022.104034.

19 M. Mehmandoust, G. Li and N. Erk, Biomass-Derived Carbon Materials as an Emerging Platform for Advanced Electrochemical Sensors: Recent Advances and Future Perspectives, *Ind. Eng. Chem. Res.*, 2023, **62**(11), 4628–4635, DOI: 10.1021/acs.iecr.2c03058.

20 R. S. Varma, Biomass-Derived Renewable Carbonaceous Materials for Sustainable Chemical and Environmental Applications, *ACS Sustain. Chem. Eng.*, 2019, **7**(7), 6458–6470, DOI: 10.1021/acssuschemeng.8b06550.

21 J. Serafin, K. Kishibayev, R. Tokpayev, T. Khavaza, A. Atchabarova, Z. Ibraimov, M. Nauryzbayev, J. S. Nazzal, L. Giraldo and J. C. Moreno-Piraján, Functional Activated Biocarbons Based on Biomass Waste for CO_2 Capture and Heavy Metal Sorption, *ACS Omega*, 2023, **8**(50), 48191–48210, DOI: 10.1021/acsomega.3c07120.

22 S. M. Shaheen, P. S. Hooda and C. D. Tsadilas, Opportunities and Challenges in the Use of Coal Fly Ash for Soil Improvements – A Review, *J. Environ. Manage.*, 2014, **145**, 249–267, DOI: 10.1016/j.jenvman.2014.07.005.

23 J. Ahmad, K. J. Kontoleon, A. Majdi, M. T. Naqash, A. F. Deifalla, N. Ben Kahla, H. F. Isleem and S. M. A. Qaidi, A Comprehensive Review on the Ground Granulated Blast Furnace Slag (GGBS) in Concrete Production, *Sustainability*, 2022, **14**(14), 8783, DOI: 10.3390/su14148783.

24 S. Biswas and A. Chowdhury, Organic Supercapacitors as the Next Generation Energy Storage Device: Emergence, Opportunity, and Challenges, *ChemPhysChem*, 2023, **24**(3), e202200567, DOI: 10.1002/cphc.202200567.

25 B. Pal, S. Yang, S. Ramesh, V. Thangadurai and R. Jose, Electrolyte Selection for Supercapacitive Devices: A Critical Review, *Nanoscale Adv.*, 2019, **1**(10), 3807–3835, DOI: 10.1039/C9NA00374F.

26 J. Xiao, H. Zhan, X. Wang, Z.-Q. Xu, Z. Xiong, K. Zhang, G. P. Simon, J. Z. Liu and D. Li, Electrolyte Gating in Graphene-Based Supercapacitors and Its Use for Probing

38050 | *J. Mater. Chem. A*, 2025, **13**, 38039–38052

This journal is © The Royal Society of Chemistry 2025

Nanoconfined Charging Dynamics, *Nat. Nanotechnol.*, 2020, **15**(8), 683–689, DOI: 10.1038/s41565-020-0704-7.

27 M. Z. Iqbal, S. Zakar and S. S. Haider, Role of Aqueous Electrolytes on the Performance of Electrochemical Energy Storage Device, *J. Electroanal. Chem.*, 2020, **858**, 113793, DOI: 10.1016/j.jelechem.2019.113793.

28 C. Zhong, Y. Deng, W. Hu, J. Qiao, L. Zhang and J. Zhang, A Review of Electrolyte Materials and Compositions for Electrochemical Supercapacitors, *Chem. Soc. Rev.*, 2015, **44**(21), 7484–7539, DOI: 10.1039/C5CS00303B.

29 M. T. Ilyas, A. Fazal, Z. U. Rehman, M. A. Raza, B. S. Almutairi, M. J. Iqbal and S. Ali, Substantial Performance of Copper Sulfide Nanotubes at High Current Densities for Energy Storage Applications, *J. Energy Storage*, 2024, **85**, 111055, DOI: 10.1016/j.est.2024.111055.

30 W. Qin, N. Zhou, C. Wu, M. Xie, H. Sun, Y. Guo and L. Pan, Mini-Review on the Redox Additives in Aqueous Electrolyte for High Performance Supercapacitors, *ACS Omega*, 2020, **5**(8), 3801–3808, DOI: 10.1021/acsomega.9b04063.

31 A. Mendhe and H. S. Panda, A Review on Electrolytes for Supercapacitor Device, *Discov. Mater.*, 2023, **3**(1), 29, DOI: 10.1007/s43939-023-00065-3.

32 S. R. Gurav, S. A. Sawant, G. R. Chodankar, U. V. Shembade, A. V. Moholkar and R. G. Sonkawade, Exploration of Aqueous Electrolyte on the Interconnected Petal-like Structure of Co-MOFs for High-Performance Paper-Soaked Supercapacitors, *Electrochim. Acta*, 2023, **467**, 143027, DOI: 10.1016/j.electacta.2023.143027.

33 G. A. Giffin, The Role of Concentration in Electrolyte Solutions for Non-Aqueous Lithium-Based Batteries, *Nat. Commun.*, 2022, **13**(1), 5250, DOI: 10.1038/s41467-022-32794-z.

34 S. Sharma and P. Chand, Supercapacitor and Electrochemical Techniques: A Brief Review, *Results Chem.*, 2023, **5**, 100885, DOI: 10.1016/j.rechem.2023.100885.

35 H. Wu, X. Wang, L. Jiang, C. Wu, Q. Zhao, X. Liu, B. Hu and L. Yi, The Effects of Electrolyte on the Supercapacitive Performance of Activated Calcium Carbide-Derived Carbon, *J. Power Sources*, 2013, **226**, 202–209, DOI: 10.1016/j.jpowsour.2012.11.014.

36 P. Yadav, M. K. Raju, R. K. Samudrala, M. Gangadhar, J. Pani, H. Borkar and P. A. Azeem, Cost-Effective Akermanite Derived from Industrial Waste for Working Electrodes in Supercapacitor Applications, *New J. Chem.*, 2023, **47**(7), 3255–3265, DOI: 10.1039/D2NJ05066H.

37 P. Yadav and P. Abdul Azeem, Green Synthesis of Calcium Magnesium Silicate Using Industrial Waste Material, *Mater. Today Proc.*, 2023, **102**, 278–282, DOI: 10.1016/j.matpr.2023.05.094.

38 P. Yadav, P. A. Azeem, S. Patel, G. Mahar, R. Yadav and H. Borkar, Novel Industrial Biomass Derived Materials for Super Capacitor Application in Powering up Electronic Gadgets, *J. Energy Storage*, 2024, **97**, 112653, DOI: 10.1016/j.est.2024.112653.

39 A. Goswami, D. Ghosh, D. Pradhan and K. Biradha, In Situ Grown Mn(II) MOF upon Nickel Foam Acts as a Robust Self-Supporting Bifunctional Electrode for Overall Water Splitting: A Bimetallic Synergistic Collaboration Strategy, *ACS Appl. Mater. Interfaces*, 2022, **14**(26), 29722–29734, DOI: 10.1021/acsami.2c04304.

40 H. Shao, Z. Lin, K. Xu, P.-L. Taberna and P. Simon, Electrochemical Study of Pseudocapacitive Behavior of Ti3C2Tx MXene Material in Aqueous Electrolytes, *Energy Storage Mater.*, 2019, **18**, 456–461, DOI: 10.1016/j.ensm.2018.12.017.

41 Y. Liu, S. P. Jiang and Z. Shao, Intercalation Pseudocapacitance in Electrochemical Energy Storage: Recent Advances in Fundamental Understanding and Materials Development, *Mater. Today Adv.*, 2020, **7**, 100072, DOI: 10.1016/j.mtadv.2020.100072.

42 J. N. Hausmann, B. Traynor, R. J. Myers, M. Driess and P. W. Menezes, The PH of Aqueous NaOH/KOH Solutions: A Critical and Non-Trivial Parameter for Electrocatalysis, *ACS Energy Lett.*, 2021, **6**(10), 3567–3571, DOI: 10.1021/acsenergylett.1c01693.

43 M. Liu, J. Niu, Z. Zhang, M. Dou and F. Wang, Potassium Compound-Assistant Synthesis of Multi-Heteroatom Doped Ultrathin Porous Carbon Nanosheets for High Performance Supercapacitors, *Nano Energy*, 2018, **51**, 366–372, DOI: 10.1016/j.nanoen.2018.06.037.

44 B. Pal, S. Yang, S. Ramesh, V. Thangadurai and R. Jose, Electrolyte Selection for Supercapacitive Devices: A Critical Review, *Nanoscale Adv.*, 2019, **1**(10), 3807–3835, DOI: 10.1039/C9NA00374F.

45 M. M. Vadiyar, S. C. Bhise, S. K. Patil, S. S. Kolekar, J. Chang and A. V. Ghule, Comparative Study of Individual and Mixed Aqueous Electrolytes with ZnFe 2 O 4 Nano–Flakes Thin Film as an Electrode for Supercapacitor Application, *ChemistrySelect*, 2016, **1**(5), 959–966, DOI: 10.1002/slct.201600151.

46 P. Samanta, S. Ghosh, N. Chandra Murmu and T. Kuila, Effect of Redox Additive in Aqueous Electrolyte on the High Specific Capacitance of Cation Incorporated MnCo2O4@Ni(OH)2 Electrode Materials for Flexible Symmetric Supercapacitor, *Composites, Part B*, 2021, **215**, 108755, DOI: 10.1016/j.compositesb.2021.108755.

47 M. Jayachandran, A. Rose, T. Maiyalagan, N. Poongodi and T. Vijayakumar, Effect of Various Aqueous Electrolytes on the Electrochemical Performance of α-MnO2 Nanorods as Electrode Materials for Supercapacitor Application, *Electrochim. Acta*, 2021, **366**, 137412, DOI: 10.1016/j.electacta.2020.137412.

48 M. M. Vadiyar, S. C. Bhise, S. K. Patil, S. S. Kolekar, A. R. Shelke, N. G. Deshpande, J.-Y. Chang, K. S. Ghule and A. V. Ghule, Contact Angle Measurements: A Preliminary Diagnostic Tool for Evaluating the Performance of ZnFe 2 O 4 Nano-Flake Based Supercapacitors, *Chem. Commun.*, 2016, **52**(12), 2557–2560, DOI: 10.1039/C5CC08373G.

49 M. Kazazi, High-Performance Electrode Based on Electrochemical Polymerization of Polypyrrole Film on Electrophoretically Deposited CNTs Conductive Framework for Supercapacitors, *Solid State Ionics*, 2019, **336**, 80–86, DOI: 10.1016/j.ssi.2019.03.021.

This journal is © The Royal Society of Chemistry 2025

J. Mater. Chem. A, 2025, **13**, 38039–38052 | **38051**

50 B. Pattanayak, P.-A. Le, D. Panda, F. M. Simanjuntak, K.-H. Wei, T. Winie and T.-Y. Tseng, Ion Accumulation-Induced Capacitance Elevation in a Microporous Graphene-Based Supercapacitor, *RSC Adv.*, 2022, **12**(42), 27082–27093, DOI: **10.1039/D2RA04194D**.

51 T. Ying, Y. Jing-Wang, X. Rong and Y. Bao-Lian, Influence of Electrolyte Concentration and Temperature on the Capacitance of Activated Carbon, *Acta Phys.-Chim. Sin.*, 2011, **27**(02), 479–485, DOI: **10.3866/PKU.WHXB20110221**.

52 R. Mondal, N. K. Mishra, T. Maiyalagan, A. Gupta and P. Singh, La 1− x K x FeO 3−δ : An Anion Intercalative Pseudocapacitive Electrode for Supercapacitor Application, *ACS Omega*, 2021, **6**(45), 30488–30498, DOI: **10.1021/acsomega.1c03902**.

53 P. Yadav, S. Patel, G. Mahar, V. Sharma, Satish, M. Kakunuri, I. Syed and P. A. Azeem, Enhancing the Performance of Industrial Waste-Based Supercapacitor by Laser Scribing for Energy Storage Applications, *J. Electroanal. Chem.*, 2025, **996**, 119404, DOI: **10.1016/j.jelechem.2025.119404**.

54 M. A. A. Mohd Abdah, N. H. N. Azman, S. Kulandaivalu and Y. Sulaiman, Asymmetric Supercapacitor of Functionalised Electrospun Carbon Fibers/Poly(3,4-Ethylenedioxythiophene)/Manganese Oxide//Activated Carbon with Superior Electrochemical Performance, *Sci. Rep.*, 2019, **9**(1), 16782, DOI: **10.1038/s41598-019-53421-w**.

55 W. Wang, S. Guo, I. Lee, K. Ahmed, J. Zhong, Z. Favors, F. Zaera, M. Ozkan and C. S. Ozkan, Hydrous Ruthenium Oxide Nanoparticles Anchored to Graphene and Carbon Nanotube Hybrid Foam for Supercapacitors, *Sci. Rep.*, 2014, **4**(1), 4452, DOI: **10.1038/srep04452**.

56 M. Mondal, D. K. Goswami and T. K. Bhattacharyya, Lignocellulose Based Bio-Waste Materials Derived Activated Porous Carbon as Superior Electrode Materials for High-Performance Supercapacitor, *J. Energy Storage*, 2021, **34**, 102229, DOI: **10.1016/j.est.2020.102229**.

57 A. T. S. C. Brandão, S. State, R. Costa, P. Potorac, J. A. Vázquez, J. Valcarcel, A. F. Silva, L. Anicai, M. Enachescu and C. M. Pereira, Renewable Carbon Materials as Electrodes for High-Performance Supercapacitors: From Marine Biowaste to High Specific Surface Area Porous Biocarbons, *ACS Omega*, 2023, **8**(21), 18782–18798, DOI: **10.1021/acsomega.3c00816**.

58 L. Pandey, S. Sarkar, A. Arya, A. L. Sharma, A. Panwar, R. K. Kotnala and A. Gaur, Fabrication of Activated Carbon Electrodes Derived from Peanut Shell for High-Performance Supercapacitors, *Biomass Convers. Biorefin.*, 2023, **13**(8), 6737–6746, DOI: **10.1007/s13399-021-01701-9**.

59 J. Yu, N. Fu, J. Zhao, R. Liu, F. Li, Y. Du and Z. Yang, High Specific Capacitance Electrode Material for Supercapacitors Based on Resin-Derived Nitrogen-Doped Porous Carbons, *ACS Omega*, 2019, **4**(14), 15904–15911, DOI: **10.1021/acsomega.9b01916**.

60 R. I. M. Vitto, M. T. Natividad and S. T. Palisoc, High-Performance and Low-Cost Coin-Cell Supercapacitors Based on Waste Graphite from Spent Dry-Cell Batteries, *J. Power Sources*, 2023, **582**, 233547, DOI: **10.1016/j.jpowsour.2023.233547**.

38052 | *J. Mater. Chem. A*, 2025, **13**, 38039–38052

This journal is © The Royal Society of Chemistry 2025